

Research Paper

Composition-Tunable Ultrasmall Manganese Ferrite Nanoparticles: Insights into their *In Vivo* T₁ Contrast Efficacy

Yuqing Miao^{1*}, Qian Xie^{2*}, Huan Zhang¹, Jing Cai³, Xiaoli Liu¹, Ju Jiao⁴, Shanshuang Hu⁵, Anujit Ghosal¹, Yu Yang⁵, Haiming Fan¹✉

1. Key Laboratory of Synthetic and Natural Functional Molecule Chemistry of the Ministry of Education, College of Chemistry and Materials Science, Northwest University, Xi'an, Shaanxi 710069, China.
2. Division of nephrology, Peking University Third Hospital, Beijing, China.
3. State Key Laboratory of Oncology in South China, Sun Yat-sen University Cancer Center, Collaborative Innovation Center for Cancer Medicine, Guangzhou 510060, China.
4. Department of Nuclear Medicine, The Third Affiliated Hospital of Sun Yat-sen University, 600 Tianhe Road, Guangzhou, Guangdong 510630, China.
5. School of Life Sciences, National Engineering Research Center for Miniaturized Detection Systems, Northwest University, Xi'an, Shaanxi, China.

*Yuqing Miao and Qian Xie have equal contribution.

✉ Corresponding author: fanhm@nwu.edu.cn

© Ivyspring International Publisher. This is an open access article distributed under the terms of the Creative Commons Attribution (CC BY-NC) license (<https://creativecommons.org/licenses/by-nc/4.0/>). See <http://ivyspring.com/terms> for full terms and conditions.

Received: 2018.11.04; Accepted: 2019.01.22; Published: 2019.02.28

Abstract

The development of a highly efficient, low-toxicity, ultrasmall ferrite nanoparticle-based T₁ contrast agent for high-resolution magnetic resonance imaging (MRI) is highly desirable. However, the correlations between the chemical compositions, *in vitro* T₁ relaxivities, *in vivo* nano-bio interactions and toxicities remain unclear, which has been a challenge in optimizing the *in vivo* T₁ contrast efficacy.

Methods: Ultrasmall (3 nm) manganese ferrite nanoparticles (Mn_xFe_{3-x}O₄) with different doping concentrations of the manganese ions (x = 0.32, 0.37, 0.75, 1, 1.23 and 1.57) were used as a model system to investigate the composition-dependence of the *in vivo* T₁ contrast efficacy. The efficacy of liver-specific contrast-enhanced MRI was assessed through systematic multiple factor analysis, which included the *in vitro* T₁ relaxivity, *in vivo* MRI contrast enhancement, pharmacokinetic profiles (blood half-life time, biodistribution) and biosafety evaluations (*in vitro* cytotoxicity testing, *in vivo* blood routine examination, *in vivo* blood biochemistry testing and H&E staining to examine the liver).

Results: With increasing Mn doping, the T₁ relaxivities initially increased to their highest value of 10.35 mM⁻¹s⁻¹, which was obtained for Mn_{0.75}Fe_{2.25}O₄, and then the values decreased to 7.64 mM⁻¹s⁻¹, which was obtained for the Mn_{1.57}Fe_{1.43}O₄ nanoparticles. Nearly linear increases in the *in vivo* MRI signals (ΔSNR) and biodistributions (accumulation in the liver) of the Mn_xFe_{3-x}O₄ nanoparticles were observed for increasing levels of Mn doping. However, both the *in vitro* and *in vivo* biosafety evaluations suggested that Mn_xFe_{3-x}O₄ nanoparticles with high Mn-doping levels (x > 1) can induce significant toxicity.

Conclusion: The systematic multiple factor assessment indicated that the Mn_xFe_{3-x}O₄ (x = 0.75-1) nanoparticles were the optimal T₁ contrast agents with higher *in vivo* efficacies for liver-specific MRI than those of the other compositions of the Mn_xFe_{3-x}O₄ nanoparticles. Our work provides insight into the optimization of ultrasmall ferrite nanoparticle-based T₁ contrast agents by tuning their compositions and promotes the translation of these ultrasmall ferrite nanoparticles for clinical use of high-performance contrast-enhanced MRI.

Key words: ultrasmall ferrite nanoparticles, composition effect, MRI, *in vivo* T₁ contrast efficacy

Introduction

There has been increasing interest in the application of ultrasmall ferrite nanoparticles (UFNPs) in nanomedicine due to their uniquely appealing

magnetic resonance (MR) T₁ contrast effects [1-8]. In comparison with commercial Gd-based T₁ contrast agents, UFNPs with sizes smaller than 5 nm have

exhibited enhanced r_1 relaxivities [8] and improved biosafety [9]. Previous studies have indicated that the *in vitro* T_1 contrast ability of the UFNPs is closely correlated with their material parameters, such as size [1, 5, 10], composition [7, 11, 12] and surface chemistry [10, 13]. To achieve efficient MR T_1 contrast agents, efforts have been devoted to chemically tailoring the material parameters of UFNPs to maximizing the r_1 relaxivity. However, enhancement of the *in vitro* r_1 relaxivity alone is inadequate for generating high-performance UFNPs-based MR T_1 contrast agents. Multiple biological steps are involved in the systemic delivery of contrast agents to biological targets, and the biosafety of the agents can influence their *in vivo* T_1 contrast efficacies [9, 14-18]. In fact, both experimental results and clinical data have verified that the *in vivo* efficacies of contrast agents are determined by a complex interplay of the *in vitro* T_1 relaxivity, the *in vivo* nano-bio interactions and their toxicity. As a result, their blood circulation, biodistribution and toxicity effects are important factors to consider along with their r_1 relaxivity [19-21]. Significantly, a variation in any material parameter can alter all related factors, resulting in an unpredictable *in vivo* T_1 contrast efficacy [16]. For example, in addition to the T_1 relaxivity dependence, the proper size selection of UFNPs can prolong their blood circulation times, which in turn leads to high accumulation in targeting tissue and greater *in vivo* contrast efficacy [1, 7]. Therefore, understanding the correlations between the material parameters of UFNPs and their *in vitro* T_1 relaxivities, *in vivo* nano-bio interactions and biosafety is of importance for translating UFNPs into clinical applications.

Among the various chemically tunable material parameters of UFNPs, the UFNPs composition has been shown to have a significant impact on the T_1 relaxivities [22]. In particular, ultrasmall manganese ferrite nanoparticles (UMFNPs) can possess a larger r_1 relaxivity (up to 1.7 times greater) than that of maghemite nanoparticles of the same size. A similar composition dependence of the T_2 relaxivity has also been reported for large-sized manganese ferrite nanoparticles [23]. Moreover, higher particle accumulation in the liver has been found for UMFNPs due to Mn²⁺ doping [7], which suggests that the UMFNPs have a unique compositional effect on the *in vivo* nano-bio interactions. In addition, the release of Mn²⁺ may potentially increase the toxicity, which should be optimized [24]. However, the interplay of the Mn²⁺ composition and the *in vitro* T_1 relaxivity, *in vivo* nano-bio interactions and toxicity remains unclear, despite UMFNPs being considered potential MRI T_1 contrast agents for liver-specific MRI.

In this study, we investigated *in vivo* T_1 contrast

efficacy of composition-tunable UMFNPs to address the concerns of the tunability of *in vitro* T_1 relaxivities, *in vivo* nano-bio interactions and toxicities of UFNPs. Mn_xFe_{3-x}O₄ nanoparticles (3 nm, $x = 0.32, 0.37, 0.75, 1, 1.23$ and 1.57) were used as a model system to assess the *in vivo* liver-specific contrast efficacy of UMFNPs in mice. The surface functionalization was optimized in terms of the colloidal stability and T_1 enhancement ability using phosphorylated mPEG with different molecular weights. The compositional dependence of their *in vitro* T_1 relaxivities, pharmacokinetic behaviors and biosafety characteristics were systematically evaluated. While Mn_{0.75}Fe_{2.25}O₄ exhibited the largest r_1 relaxivity value of 10.35 mM⁻¹s⁻¹, the greatest MRI signal enhancement (Δ SNR) of the liver has been obtained by using Mn_{1.57}Fe_{1.43}O₄ due to its high liver accumulation. However, high Mn doping concentrations ($x = 1.23$ and 1.57) simultaneously induced significant cytotoxicity. The comprehensive results indicated that Mn_xFe_{3-x}O₄ nanoparticles with Mn-doping concentrations between 0.75 and 1 can exhibit high *in vivo* liver-specific contrast efficacy. This work aims to provide a clear relationship between the compositional characteristics and the *in vivo* T_1 contrast efficacy of UMFNPs. The results obtained from the current work may provide guidance for the chemical design and preclinical assessment of UFNPs-based MR T_1 contrast agents and facilitate their clinical translation.

Materials and Methods

Materials

Absolute ethanol, methanol, hexane, ferric chloride hexahydrate (> 99.0%), manganese chloride tetrahydrate (> 99.0%), sodium hydroxide (> 96%), tetrahydrofuran (> 99.0%), chloroform (> 99.0%) were used as received. Benzyl ether (98%), oleic acid (90%), oleyl alcohol (65.0%) and Poly (ethylene glycol) methyl ether (flakes, average Mn ~1,000, ~2,000 and ~5,000) were purchased from Aldrich Chemical Co. Erucic acid was purchased from Aladdin Industrial Corporation.

Synthesis of 3 nm Mn_xFe_{3-x}O₄ Nanoparticles

The iron-eruciate and manganese-oleate precursors were synthesized using previously reported procedures [7]. Mn_xFe_{3-x}O₄ nanoparticles (3 nm) were prepared by a general method for the dynamic simultaneous thermal decomposition (DSTD) of the precursors. A typical synthesis of the Mn_{0.75}Fe_{2.25}O₄ nanoparticles is briefly described as follows: 1.4 g (1.3 mmol) of the iron-eruciate complex, 0.57 g (2 mmol) of oleic acid, 0.62 g (1 mmol) of the Mn-oleate complex, and 1.61 g (6 mmol) of oleyl alcohol were dissolved in 10 g of benzyl ether. The reaction mixture magnetica-

lly stirred under a flow of argon. The reaction mixture was heated to 265 °C with a constant rate of 5 °C/min, and the kept that temperature for 30 min. The resulting solution containing the nanoparticles was then rapidly cooled to room temperature. A black powder was precipitated by the addition of ethanol to the reaction mixture and was then isolated by centrifugation. The isolated UMFNPs were dispersed in hexane for further use. UMFNPs with different Mn doping levels were prepared by mixing different ratios of the precursor under identical conditions. Detailed reaction parameters are summarized in Table 1.

Table 1. Detailed Synthetic Parameters for Ultrasmall $Mn_xFe_{3-x}O_4$ Nanoparticles

Samples	Fe-eruciate (g)	Mn-oleate (g)	Oleyl alcohol (g)	Oleic acid (g)	Benzyl Ether (g)	Heating rate (°C/min)	Aging temperature (°C)
$Mn_{0.32}Fe_{2.68}O_4$	2.14	0.62	1.61	0.57	10	5	260
$Mn_{0.37}Fe_{2.63}O_4$	1.82	0.62	1.61	0.57	10	5	260
$Mn_{0.75}Fe_{2.25}O_4$	1.40	0.62	1.61	0.57	10	5	260
$MnFe_2O_4$	1.07	0.62	1.61	0.57	10	5	260
$Mn_{1.23}Fe_{1.77}O_4$	1.07	0.93	1.61	0.57	10	5	260
$Mn_{1.57}Fe_{1.43}O_4$	1.07	1.24	1.61	0.57	10	5	260

Preparation of phosphorylated mPEG coated $Mn_xFe_{3-x}O_4$ nanoparticles

Phosphorylated mPEG was synthesized by reacting $POCl_3$ with mPEG as previously reported [25]. In a typical process, 10 mg of $Mn_xFe_{3-x}O_4$ nanoparticles and 50 mg of phosphorylated mPEG were transferred into 10 mL of chloroform. Next, the mixture was shaken continuously over a period of 5 h to remove the chloroform and obtain functionalized UMFNPs. Finally, 5 ml of water was added to redisperse the nanoparticles, and passed through a 0.22 μ m syringe filter and stored at 4 °C until use.

Characterization

X-ray powder diffraction studies patterns were obtained with a Bruker D8 Advanced Diffractometer System equipped with $Cu/K\alpha$ radiation ($\lambda = 1.5418$ Å). Transmission electron microscopy (TEM) images were obtained on a field-emission transmission electron microscope (Tecnica G2 F20 S-Twin, FEL, operated at 200 kV). The mean particle sizes were obtained from digital TEM images by counting more than 200 particles. Magnetic properties studies were carried out using a superconducting quantum interference device (SQUID) magnetometer (MPMS-XL-7) with the magnetic field up to 3 T. The hydrodynamic diameters of the UMFNPs were measured by Malvern Zetasizer nano-ZS dynamic light scattering (DLS) instrument. The metal elemental analyses of the samples were performed on inductively coupled plasma atomic emission spectroscopy (ICP-AES) and

ICP-MS (PerkinElmer SCIEX, ELAN DRC-e).

Relaxivity Measurements

MR relaxivities of UMFNPs were carried out on an MRI scanner with a head coil at 3 T (Siemens Medical Solutions, Germany). The parameters for T_1 measurement were set as: echo time (TE) = 19 ms, repetition time (TR) = 4000 ms, and TI = 25, 50, 100, 200, 300, 400, 500, 700, 1000, 1500, 2500, 3500 ms, respectively. For T_2 relaxivity measurements, the parameters were set as: repetition time (TR) = 5000 ms and echo time (TE) = 13, 30, 92, 113, 141, 170, 198, 210, 240, 278, 322 ms.

MR imaging of liver *in vivo*

The MR images were acquired on a 3.0 T clinical MRI instrument (Siemens Trio). UMFNPs (3 mg [Fe+Mn]/kg) were injected into the mice for liver imaging. T_1 -weighted MR images of their livers were obtained at designed time points. The detailed parameters for T_1 imaging were set as follows: field of view (FOV) = 40 × 80 mm²; flip angle (FA) = 120; slice thickness = 3.0 mm; TR = 485 ms; TE = 10 ms; number of excitations (NEX) = 12. *In vivo* experiments were carried out according to protocol approved by the Institutional Animal Care and Use Committee of Sun Yat-sen University.

Biodistribution and Pharmacokinetics Studies

Balb/c mice were injected intravenously with the $Mn_xFe_{3-x}O_4$ nanoparticles at a dose of 3 mg [Fe+Mn]/kg mouse body weight to evaluate the biodistribution of the nanoparticles. The mice were sacrificed at 3 h and 24 h post injection (p.i.). The organs of interest (brain, lung, heart, kidney, spleen and liver) were harvested, weighed and quantified using ICP-MS. To determine the pharmacokinetic parameters, mice were injected with $Mn_xFe_{3-x}O_4$ nanoparticles and blood samples were collected at 2 min, 5 min, 10 min, 30 min, 1 h, 3 h, 5 h, 8 h, 12 h, and 24 h p.i. and quantified using ICP-MS. The pharmacokinetic parameters were calculated based on a two-compartment open model.

Results and Discussion

Synthesis of composition tunable UMFNPs

The $Mn_xFe_{3-x}O_4$ nanoparticles were synthesized *via* a DSTD method [7]. The Mn content ($x = 0.32, 0.37, 0.75, 1, 1.23$ and 1.57) in the UMFNPs could be controlled by changing the ratios of the precursors. Figure 1a-f shows the TEM images of as-prepared $Mn_xFe_{3-x}O_4$ nanoparticles with different Mn content. All samples show a uniform particle size of 3 nm with narrow size distributions (< 4%) (Figure S1). The corresponding high-resolution TEM (HRTEM) images

are shown in the inset of Figure 1a-f, revealing the high crystallinities of these particles. The lattice spacing distances are found to be 2.12 Å, 2.45 Å, 2.56 Å, 2.45 Å, 2.12 Å and 3.01 Å, which correspond to the (400), (222), (311), (222), (400) and (220) planes, respectively, of the inverse spinel phase of manganese ferrite. Figure 1g shows the powder X-ray diffraction (XRD) patterns of the as-synthesized ultrasmall $\text{Mn}_x\text{Fe}_{3-x}\text{O}_4$ nanoparticles. The position of all diffraction peaks matches well with the standard manganese ferrite powder diffraction data (JCPDS card no. 10-0319). The ICP-AES elemental analysis revealed the tunable-ratios of Mn:Fe in $\text{Mn}_x\text{Fe}_{3-x}\text{O}_4$ can be 0.32:2.68, 0.37:2.63, 0.75:2.25, 1:2, 1.23:1.77 and 1.57:1.43, which are consistent with the results measured by using energy dispersive X-ray spectroscopy (EDS; Figure S2 and Table S1 in the Supporting Information). The as-prepared $\text{Mn}_x\text{Fe}_{3-x}\text{O}_4$ nanoparticles were further analyzed by X-ray photoelectron spectroscopy (XPS) (Figure 1h and 1i). The binding

energies at 711.9 and 725.8 eV for $\text{Mn}_{0.32}\text{Fe}_{2.68}\text{O}_4$, 711.0 and 724.3 eV for $\text{Mn}_{0.37}\text{Fe}_{2.63}\text{O}_4$, 711.8 and 724.7 eV for $\text{Mn}_{0.75}\text{Fe}_{2.25}\text{O}_4$, 711.8 and 725.5 eV for MnFe_2O_4 , 710.9 and 725.1 eV for $\text{Mn}_{1.23}\text{Fe}_{1.77}\text{O}_4$, and 711.2 and 724.8 eV for $\text{Mn}_{1.57}\text{Fe}_{1.43}\text{O}_4$ are attributed to Fe 2p_{3/2} and Fe 2p_{1/2} referred to Fe^{3+} , respectively. The photoelectron peaks at binding energies of Mn 2p_{3/2} and Mn 2p_{1/2} were 642.6 and 654.4 eV for $\text{Mn}_{0.32}\text{Fe}_{2.68}\text{O}_4$, 642.0 and 653.9 eV for $\text{Mn}_{0.37}\text{Fe}_{2.63}\text{O}_4$, 642.4 and 654.5 eV for $\text{Mn}_{0.75}\text{Fe}_{2.25}\text{O}_4$, 642.1 and 653.9 eV for MnFe_2O_4 , 641.8 and 653.7 eV for $\text{Mn}_{1.23}\text{Fe}_{1.77}\text{O}_4$, and 641.6 and 653.2 eV for $\text{Mn}_{1.57}\text{Fe}_{1.43}\text{O}_4$, respectively (Table S2). The peak positions of Fe 2p and Mn 2p are consistent with previously reported values for Fe^{3+} and Mn^{2+} [7, 23, 26]. With increasing Mn^{2+} , the intensities of the Fe 2p peaks decrease, and those of the Mn 2p peaks increase, which is consistent with the literature results [27]. These data suggest that 3 nm $\text{Mn}_x\text{Fe}_{3-x}\text{O}_4$ nanoparticles, where $x = 0.32, 0.37, 0.75, 1, 1.23$ and 1.57 , were successfully synthesized by the DSTD method.

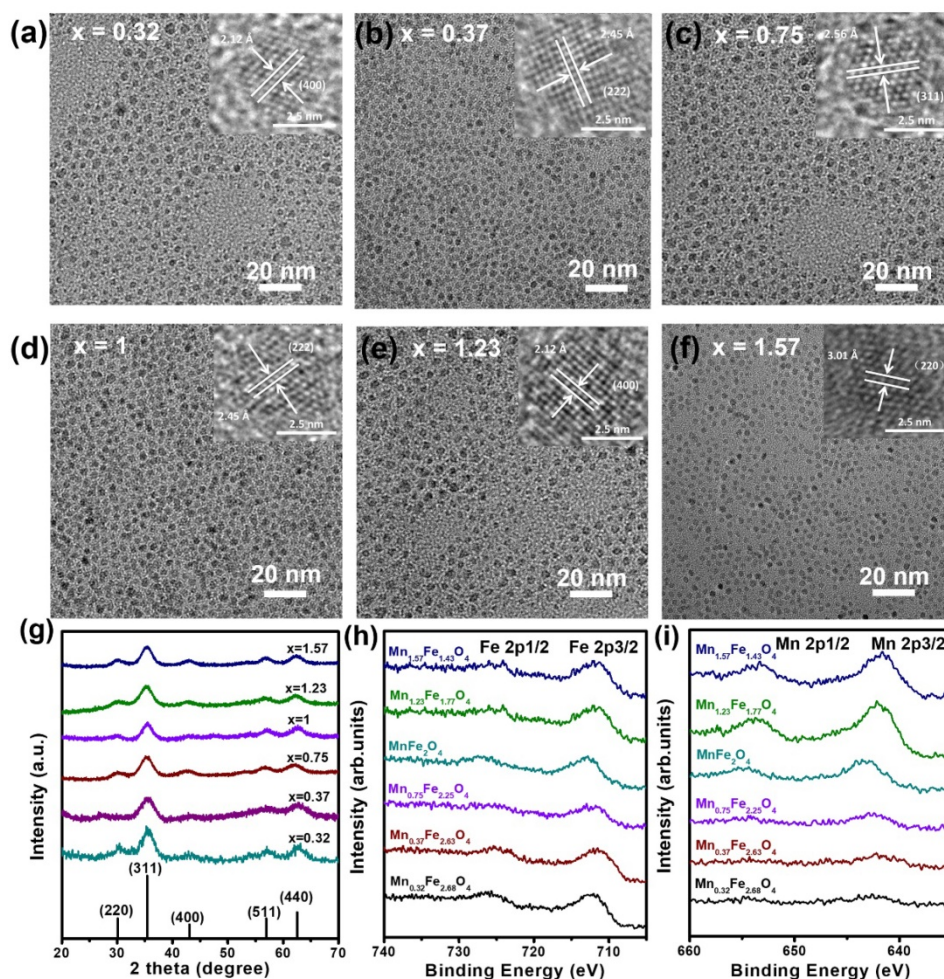


Figure 1. (a-f) TEM images of ultrasmall $\text{Mn}_x\text{Fe}_{3-x}\text{O}_4$ nanoparticles. The insets are the high-resolution TEM images. (g) XRD patterns of ultrasmall $\text{Mn}_x\text{Fe}_{3-x}\text{O}_4$ nanoparticles. XPS spectra of ultrasmall $\text{Mn}_x\text{Fe}_{3-x}\text{O}_4$ nanoparticles, (h) Fe 2p and (i) Mn 2p.

Magnetic characterization

The magnetic properties of UMFNPs are strongly associated with their MR relaxivity properties. The magnetic properties of these $Mn_xFe_{3-x}O_4$ nanoparticles were measured using a superconducting quantum interference device (SQUID) with the field up to 3 T. Figure 2a shows the field-dependent magnetization (M-H) curves of the ultrasmall $Mn_xFe_{3-x}O_4$ nanoparticles at 300 K. The coercivity and remanence are negligible at room temperature for all these samples, indicating superparamagnetic behavior. The variations in magnetization as a function of the Mn-doping concentration are presented in Figure 2b. The magnetizations at 3 T are 21.78, 31.07, 26.92, 25.59, 10.69, and 8.20 emu/g for the $Mn_{0.32}Fe_{2.68}O_4$, $Mn_{0.37}Fe_{2.63}O_4$, $Mn_{0.75}Fe_{2.25}O_4$, $MnFe_2O_4$, $Mn_{1.23}Fe_{1.77}O_4$ and $Mn_{1.57}Fe_{1.43}O_4$ nanoparticles, respectively. The magnetization was found to initially increase by up to 42% with the increase of x up to 0.37. Metal ferrite nanoparticles has a spinel structure constructed by face-centered cubic packed lattice of oxygen atoms with the tetrahedral sites and octahedral sites [28, 29]. It is well known that $MnFe_2O_4$ has a mixed spinel structure with the manganese ions predominantly occupying tetrahedral sites. Mn^{2+} has five unpaired electrons, which is the same number as in Fe^{3+} , and one more than in Fe^{2+} . When an external magnetic field is applied, the magnetic spins of the O_h sites align parallel to the direction of the external magnetic field, but those of the T_d sites align antiparallel to the field. For $Mn_xFe_{3-x}O_4$ nanoparticles with small x values, the Mn^{2+} dopant can replace Fe^{2+} to give a magnetic moment of $(4+x) \mu_B$ (Bohr magneton) per formula unit, resulting in an enhanced magnetic moment in comparison with $[Fe^{3+}]_{Td}[Fe^{2+}Fe^{3+}]_{Oh}O_4$. However, as the doping level further increases, the magnetization gradually decreases to 8.20 emu/g ($x = 1.57$) due to the weakening of the T_d - O_h interaction when Fe^{3+} is replaced by Mn^{2+} in the T_d site [30-32]. Similar results have been observed in large-sized manganese ferrite nanoparticles [23, 31].

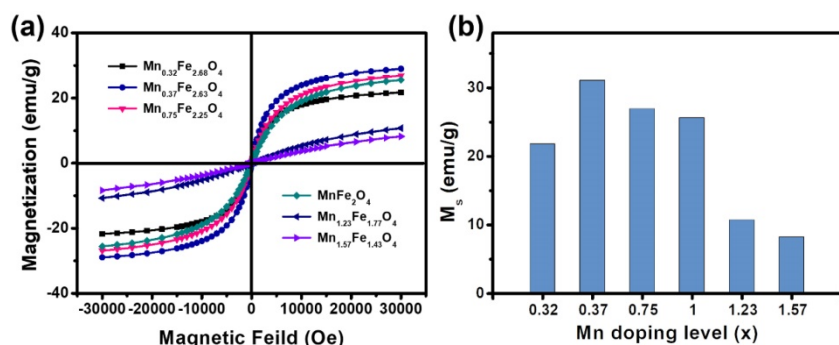


Figure 2. Magnetic characterization of 3 nm $Mn_xFe_{3-x}O_4$ nanoparticles. **(a)** Field-dependent magnetization curves (M-H) of ultrasmall $Mn_xFe_{3-x}O_4$ nanoparticles at 300 K. **(b)** The magnetizations at 3 T of the ultrasmall $Mn_xFe_{3-x}O_4$ samples.

Surface modification of the $Mn_xFe_{3-x}O_4$ nanoparticles

Appropriate surface coatings for $Mn_xFe_{3-x}O_4$ nanoparticle-based contrast agents are necessary for improved dispersibilities and T_1 contrast abilities. Stoichiometric $MnFe_2O_4$ nanoparticles were modified by various mPEG with molecular weights of 1000, 2000 and 5000 g/mol followed by evaluation of their colloidal stabilities and *in vitro* T_1 relaxivities. Figure 3a-c shows the hydrodynamic sizes of the $MnFe_2O_4$ nanoparticles modified with mPEG1000, mPEG2000 and mPEG5000, respectively. The hydrodynamic sizes in deionized water are seen to be 8.74 nm for $MnFe_2O_4@mPEG1000$, 9.36 nm for $MnFe_2O_4@mPEG2000$ and 9.87 nm for $MnFe_2O_4@mPEG5000$. No observable aggregation could be seen under the optical microscope as shown in the insets of Figure 3a-c. Figure 3d-f shows the time-dependent curves for the hydrodynamic sizes of the mPEG-modified $MnFe_2O_4$ nanoparticles. It can be seen that $MnFe_2O_4@mPEG1000$ and $MnFe_2O_4@mPEG2000$ do not show any significant changes in their hydrodynamic sizes after 10 days of incubation in aqueous media at room temperature, while the hydrodynamic size of $MnFe_2O_4@mPEG5000$ exhibits a significant increase after the 2nd day. The thermogravimetric analysis (TGA) results (Figure S3 and Table S3) indicate that the surface density of $MnFe_2O_4@mPEG5000$ was much less than those of $MnFe_2O_4@mPEG1000$ and $MnFe_2O_4@mPEG2000$ for the same preparation procedures. This may result in the mPEG5000-coated nanoparticles having poor aqueous stability and dispersibility. The results imply that the $MnFe_2O_4$ nanoparticles modified by mPEG1000 and mPEG2000 can achieve excellent colloidal stabilities compared to $MnFe_2O_4@mPEG5000$. The effects of the surface ligands of the $MnFe_2O_4$ nanoparticles on their MR relaxivities was further evaluated on a clinical 3 T MRI scanner at room temperature. A series of aqueous solutions of the nanoparticles with different [Fe+Mn] concentrations were prepared. Figure 3g

shows the T_1 -weighted MR images of $MnFe_2O_4@mPEG1000$, $MnFe_2O_4@mPEG2000$ and $MnFe_2O_4@mPEG5000$ at different [Fe+Mn] concentration. All of the samples with higher concentration produce brighter images, indicating that the $MnFe_2O_4@mPEG1000$, $MnFe_2O_4@mPEG2000$ and $MnFe_2O_4@mPEG5000$ samples can effectively shorten T_1 relaxation time of the water protons. However, $MnFe_2O_4@mPEG1000$ exhibits brighter images at all designated [Fe+Mn] concentrations in

comparison with $\text{MnFe}_2\text{O}_4@\text{mPEG}2000$ and $\text{MnFe}_2\text{O}_4@\text{mPEG}5000$. The r_1 relaxivities of the $\text{MnFe}_2\text{O}_4@\text{mPEG}1000$, $\text{MnFe}_2\text{O}_4@\text{mPEG}2000$ and $\text{MnFe}_2\text{O}_4@\text{mPEG}5000$ samples were 10.21, 8.46, and 8.26 $\text{mM}^{-1}\text{s}^{-1}$, respectively (Figure 3h). The r_2 relaxivities of $\text{MnFe}_2\text{O}_4@\text{mPEG}1000$, $\text{MnFe}_2\text{O}_4@\text{mPEG}2000$ and $\text{MnFe}_2\text{O}_4@\text{mPEG}5000$ were 21.27, 21.52, and 38.64 $\text{mM}^{-1}\text{s}^{-1}$, respectively (Figure S4b). Figure 3i shows the r_1 and the r_2/r_1 curves of the MnFe_2O_4 samples with different mPEG coatings. The $\text{MnFe}_2\text{O}_4@\text{mPEG}1000$ sample exhibits the highest r_1 relaxivity and the lowest r_2/r_1 value of the three samples, indicating that mPEG1000 is the optimal coating for the $\text{Mn}_x\text{Fe}_{3-x}\text{O}_4$ nanoparticles. Thus, mPEG1000 was used to modify the $\text{Mn}_x\text{Fe}_{3-x}\text{O}_4$ nanoparticles to further investigate their *in vivo* T_1 contrast efficacy.

The *in vitro* T_1 contrast ability of the ultrasmall $\text{Mn}_x\text{Fe}_{3-x}\text{O}_4$ nanoparticles

In vitro T_1 contrast ability refers to the r_1 relaxivity, which is the efficiency of a millimole of $\text{Mn}_x\text{Fe}_{3-x}\text{O}_4$ nanoparticles for enhancing the relaxation rate of water protons [33]. To determine the influence of the Mn-doping concentration on the r_1 relaxivity, the relaxometric properties of the $\text{Mn}_x\text{Fe}_{3-x}\text{O}_4$ nanoparticles were measured. 3 nm $\text{Mn}_x\text{Fe}_{3-x}\text{O}_4$

nanoparticles with different Mn-doping levels ($x = 0.32, 0.37, 0.75, 1, 1.23, 1.57$) were modified with mPEG 1000 and dispersed in deionized water. As shown in Figure 4a, the MR images enhanced by higher concentrations of UMFNPs appeared brighter than these of lower concentration. Furthermore, the T_1 -weighted MR images reveal that the $\text{Mn}_{0.75}\text{Fe}_{2.25}\text{O}_4$ nanoparticles produce the highest signal intensity among the different $\text{Mn}_x\text{Fe}_{3-x}\text{O}_4$ nanoparticles. Figure 4b shows the linear fit of the T_1 relaxation times versus the $[\text{Fe}+\text{Mn}]$ concentrations, the slope of which is the r_1 relaxivity. The r_1 relaxivity values and r_2/r_1 ratios for the different $\text{Mn}_x\text{Fe}_{3-x}\text{O}_4$ nanoparticles are presented in Figure 4c and Table S4. The *in vitro* T_1 contrast abilities of the 3 nm $\text{Mn}_x\text{Fe}_{3-x}\text{O}_4$ nanoparticles improve with increasing Mn-doping levels up to $x = 0.75$ and then decline as the Mn doping level is further increased. The maximum r_1 relaxivity is 10.35 $\text{mM}^{-1}\text{s}^{-1}$ and was obtained with the $\text{Mn}_{0.75}\text{Fe}_{2.25}\text{O}_4$ nanoparticles, while the $\text{Mn}_{1.23}\text{Fe}_{1.77}\text{O}_4$ nanoparticles exhibit the smallest r_2/r_1 ratio of 2.29 at 3 T. The results obtained from the relaxometric measurements demonstrating that ultrasmall $\text{Mn}_x\text{Fe}_{3-x}\text{O}_4$ nanoparticles ($x = 0.75-1.23$) are good candidates as T_1 MRI contrast agents.

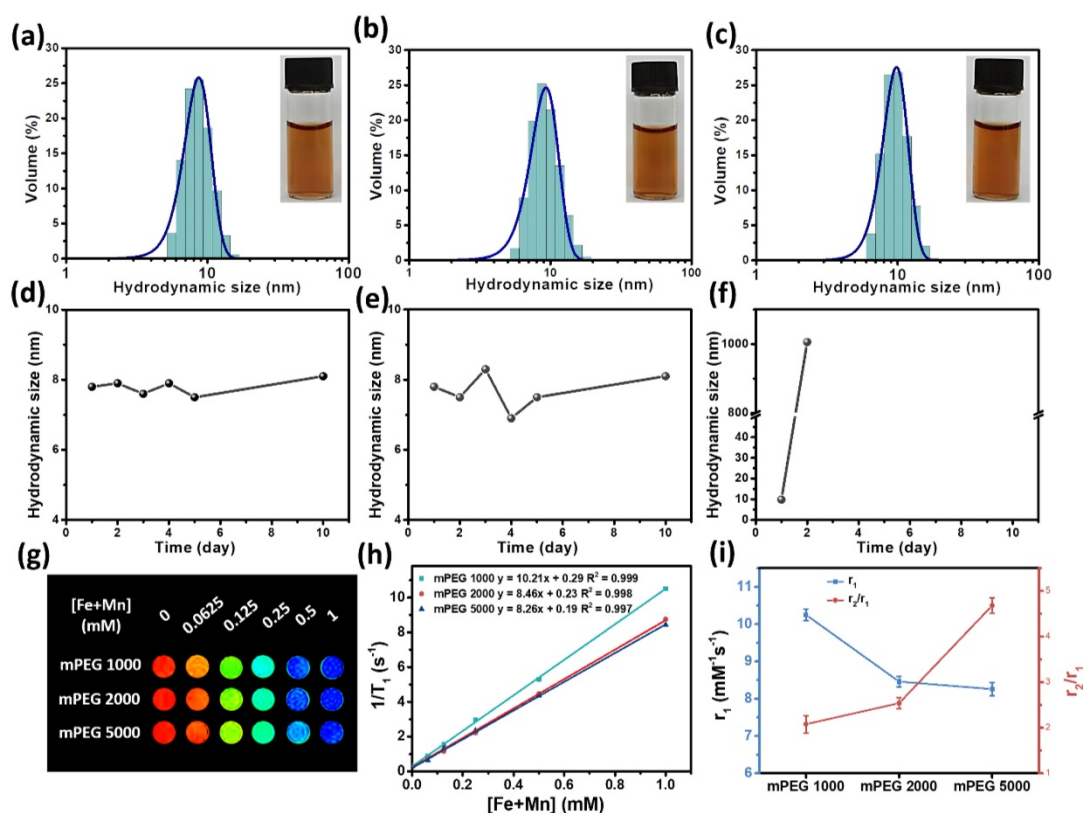


Figure 3. Hydrodynamic size of (a) $\text{MnFe}_2\text{O}_4@\text{mPEG}1000$, (b) $\text{MnFe}_2\text{O}_4@\text{mPEG}2000$, and (c) $\text{MnFe}_2\text{O}_4@\text{mPEG}5000$ in water. The insets are digital photographs of the aqueous MnFe_2O_4 nanoparticles dispersions. (d)-(f) Time-dependent hydrodynamic size of ultrasmall MnFe_2O_4 nanoparticles modified with (d) mPEG1000, (e) mPEG2000 and (f) mPEG5000, respectively. (g) T_1 -weighted phantom imaging of ultrasmall MnFe_2O_4 nanoparticles with different phosphorylated mPEG. (h) T_1 relaxation rate of the MnFe_2O_4 nanoparticles different PEG chain lengths at various $[\text{Fe}+\text{Mn}]$ concentrations. (i) r_1 value and r_2/r_1 ratio of MnFe_2O_4 nanoparticles as a function of the mPEG molecular weight.

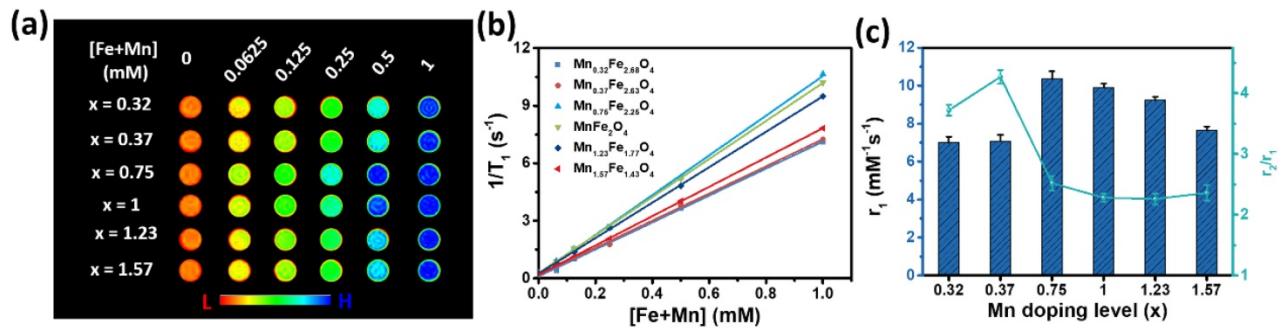


Figure 4. MR contrast effects of ultrasmall $Mn_xFe_{3-x}O_4$ nanoparticles upon changes in the Mn doping level. **(a)** T_1 -weighted images of $Mn_xFe_{3-x}O_4$ nanoparticles. **(b)** T_1 relaxation rate of the $Mn_xFe_{3-x}O_4$ nanoparticles and **(c)** r_1 relaxivities and r_2/r_1 ratio of ultrasmall $Mn_xFe_{3-x}O_4$ nanoparticles.

The mechanism of varied T_1 relaxometric properties involved in the $Mn_xFe_{3-x}O_4$ nanoparticles is attributed to a combination of the inner-sphere and outer-sphere contributions [34]. While water molecules directly coordinated to the surface ions of the nanoparticles are responsible for the inner-sphere relaxation contribution, the spin-spin interactions between the nanoparticles and the water molecules in the nearby environment affect the outer-sphere relaxation. The contrast enhancement of individual contrast agents is thus determined by both their chemical composition and magnetic properties. For T_1 contrast agents, in accordance with the classical Solomon-Bloembergen-Morgan (SBM) theory [33], the T_1 relaxivity can be given by [13]:

$$\frac{1}{T_1} = \left(\frac{1}{T_1}\right)_{inner\ sphere} + \left(\frac{1}{T_1}\right)_{outer\ sphere} \quad (1)$$

$$\left(\frac{1}{T_1}\right)_{outer\ sphere} = \frac{128\pi^2\gamma_I^2M_n}{405\rho} \left(\frac{1}{1+L/a}\right)^3 M_s^2\tau_DJ_A(\sqrt{2\omega_I\tau_D}) \quad (2)$$

$$\left(\frac{1}{T_1}\right)_{inner\ sphere} = \frac{qP_M}{T_{1M}+\tau_M} \quad (3)$$

Where ρ is the density of the $Mn_xFe_{3-x}O_4$ nanoparticles; γ_I is the gyromagnetic constant for proton; M_n is the molar mass; L refers to the thickness of surface impermeable molecule layer; M_s is the saturation magnetization of the UMFNPs; a is the particles core radius; D is the water diffusion coefficient; The translational diffusion time τ_D can be expressed as $\tau_D = r^2/D$; r equal to the a plus L ; J_A is the Ayant’s spectral density function; P_M is the molar fraction of the metal ions on the surface; q is the number of water molecules bound per metal ion; and τ_M is the residence lifetime of the bound water.

$Mn_xFe_{3-x}O_4$ nanoparticles possessing higher saturation magnetizations (M_s) result in larger r_1 relaxivities due to the increased outer-sphere contribution. The inner-sphere contribution increases with the increasing Mn^{2+} -doping level in the $Mn_xFe_{3-x}O_4$ nanoparticles due to the small τ_M of $Mn(H_2O)_6^{2+}$, which is 100 times smaller than that of $Fe(H_2O)_6^{3+}$ [33].

The overall T_1 relaxivity of a $Mn_xFe_{3-x}O_4$ nanoparticle with a certain Mn-doping level is the sum of its inner-sphere and outer-sphere contributions.

In Vivo MR Imaging

To evaluate the MRI imaging efficiency of ultrasmall $Mn_xFe_{3-x}O_4$ nanoparticles *in vivo*, Balb/c mice were used for liver-specific contrast-enhanced MRI. The samples were intravenously administrated. The experimental dose was set as 3 mg [Fe+Mn] per kilogram mouse body weight. T_1 images at transverse of the liver was acquired at 0, 3, 10, 30, 60, 90, 120, and 180 min post-injection of the $Mn_xFe_{3-x}O_4$ nanoparticles (Figure 5a). Significant signal enhancement in the T_1 -weighted MR images can be observed, demonstrating that these $Mn_xFe_{3-x}O_4$ nanoparticles can effectively accumulate in the liver. Figure 5b shows the MR signal changes in the T_1 -weighted MR images of the liver at different time points. The MR signal intensity changes were quantified using ΔSNR as calculated from the following equations:

$$SNR = SI_{mean} / SD_{noise} \quad (4)$$

$$\Delta SNR = (SNR_{post} - SNR_{pre}) / SNR_{pre} \times 100\% \quad (5)$$

where SI stands for the signal intensity and SD stands for the standard deviation [35].

The highest ΔSNR values of the contrast-enhanced MR images of the liver are $40.1 \pm 2.3\%$, $48.4 \pm 3.2\%$, $73.1 \pm 1.4\%$, $71.6 \pm 3.2\%$, $73.8 \pm 2.7\%$, and $82.2 \pm 2.1\%$, which occurred at 30 min post-injection of the $Mn_{0.32}Fe_{2.68}O_4$, $Mn_{0.37}Fe_{2.63}O_4$, $Mn_{0.75}Fe_{2.25}O_4$, $MnFe_2O_4$, $Mn_{1.23}Fe_{1.77}O_4$ and $Mn_{1.57}Fe_{1.43}O_4$ nanoparticles, respectively. The $\Delta SNRs$ increase linearly with the increasing Mn-doping levels, revealing that the *in vivo* contrast abilities in the liver of these $Mn_xFe_{3-x}O_4$ nanoparticles strongly depend on their Mn-doping level. In addition, the $Mn_{0.75}Fe_{2.25}O_4$ nanoparticles, which were expected to show a relatively large ΔSNR due to their high r_1 relaxivity of $10.36\text{ mM}^{-1}\text{s}^{-1}$, show a relatively small ΔSNR of 73.1%. The maximum ΔSNR of 82.2% was obtained using the $Mn_{1.57}Fe_{1.43}O_4$ nanoparticles, which have a relatively

low r_1 relaxivity of $7.66 \text{ mM}^{-1}\text{s}^{-1}$, which suggests that the *in vivo* contrast ability can be affected by both the T_1 relaxivities and the nano-bio interactions of $\text{Mn}_x\text{Fe}_{3-x}\text{O}_4$ nanoparticles.

Pharmacokinetics and biodistribution of the $\text{Mn}_x\text{Fe}_{3-x}\text{O}_4$ nanoparticles

The pharmacokinetics and biodistribution of the $\text{Mn}_x\text{Fe}_{3-x}\text{O}_4$ nanoparticles were then carried out to understand the effects of their *in vivo* behavior on the contrast efficacy. Figure 6a presents the concentration of the [Fe+Mn] levels in the blood after injection of the $\text{Mn}_x\text{Fe}_{3-x}\text{O}_4$ nanoparticles *via* tail vein. All the curves showed biexponential characteristics [36]. Several of the key pharmacokinetic parameters, including the distribution half-life ($t_{1/2\alpha}$), elimination half-life ($t_{1/2\beta}$), and clearance (CL), are summarized in Table S5. The distribution half-life ($t_{1/2\alpha}$) are 0.64, 0.62, 0.53, 0.50, 0.34 and 0.17 h for the $\text{Mn}_{0.32}\text{Fe}_{2.68}\text{O}_4$, $\text{Mn}_{0.37}\text{Fe}_{2.63}\text{O}_4$, $\text{Mn}_{0.75}\text{Fe}_{2.25}\text{O}_4$, MnFe_2O_4 , $\text{Mn}_{1.23}\text{Fe}_{1.77}\text{O}_4$ and $\text{Mn}_{1.57}\text{Fe}_{1.43}\text{O}_4$ nanoparticles, respectively. The elimination half-life ($t_{1/2\beta}$) are 8.01, 9.59, 10.03, 10.56, 12.7 and 17.29 h for the $\text{Mn}_{0.32}\text{Fe}_{2.68}\text{O}_4$, $\text{Mn}_{0.37}\text{Fe}_{2.63}\text{O}_4$, $\text{Mn}_{0.75}$

$\text{Fe}_{2.25}\text{O}_4$, MnFe_2O_4 , $\text{Mn}_{1.23}\text{Fe}_{1.77}\text{O}_4$ and $\text{Mn}_{1.57}\text{Fe}_{1.43}\text{O}_4$ nanoparticles, respectively. Increasing the Mn-doping concentration reduces the distribution half-life time and improves the elimination half-life time. Clearance (CL) [37–39] is a parameter used to measure the efficiency of the body toward eliminating particles through excretory or metabolic pathways. CL for $\text{Mn}_{0.32}\text{Fe}_{2.68}\text{O}_4$, $\text{Mn}_{0.37}\text{Fe}_{2.63}\text{O}_4$, $\text{Mn}_{0.75}\text{Fe}_{2.25}\text{O}_4$, MnFe_2O_4 , $\text{Mn}_{1.23}\text{Fe}_{1.77}\text{O}_4$ and $\text{Mn}_{1.57}\text{Fe}_{1.43}\text{O}_4$ nanoparticles were found to be 1, 0.67, 0.42, 0.48, 0.41 and 0.26 mL/h, respectively. As shown in Figure 6b, the CL declined with the increase of the Mn-doping concentration. This decrease in CL rate is consistent with the increase in the elimination half-life, indicating a reduced efficiency of the body toward eliminating the particles. These results explicitly suggest a dependence of half-life time and elimination on the Mn-doping level for the $\text{Mn}_x\text{Fe}_{3-x}\text{O}_4$ nanoparticles. Figure 6c and d shows the biodistributions of the $\text{Mn}_x\text{Fe}_{3-x}\text{O}_4$ nanoparticles at 3 h and 24 h postinjection. The results indicate that the $\text{Mn}_x\text{Fe}_{3-x}\text{O}_4$ nanoparticles mainly accumulate in the liver, spleen and kidney after 3 h, while the accumulation of $\text{Mn}_x\text{Fe}_{3-x}\text{O}_4$

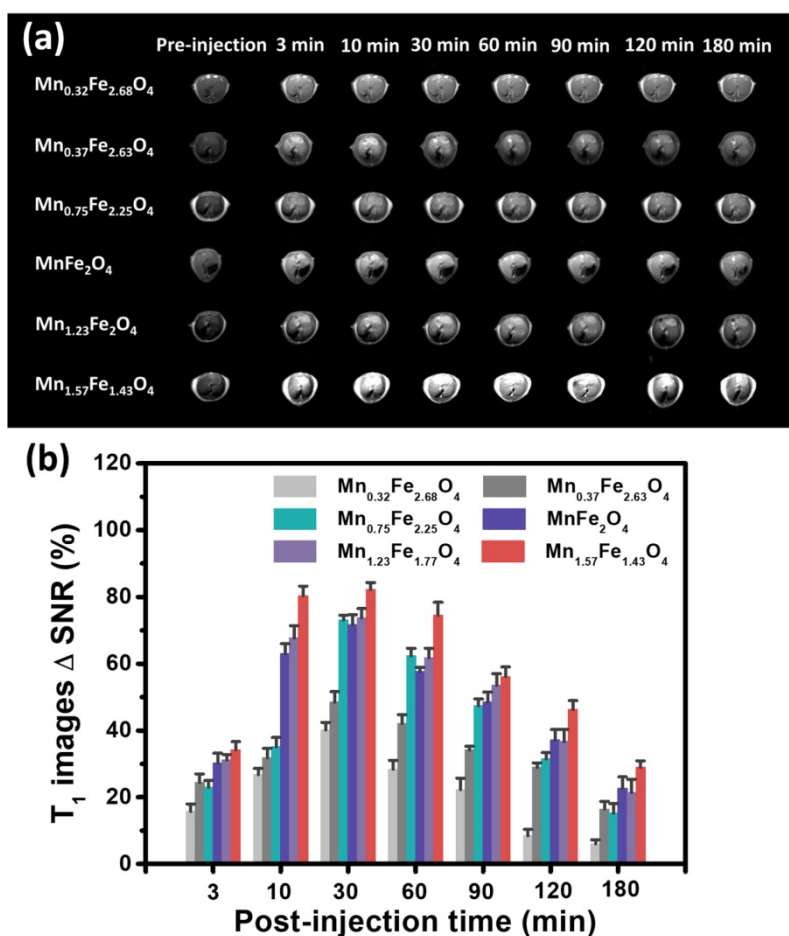


Figure 5. *In vivo* MR imaging of UMFNPs. (a) T_1 -weighted MR images of liver at 0, 3, 10, 30, 60, 90, 120, and 180 min after intravenous injection of 3 nm $\text{Mn}_x\text{Fe}_{3-x}\text{O}_4$ nanoparticles and (b) quantification analysis of MR T_1 signals changes.

nanoparticles in the liver is reduced after 24 h. The accumulation of $\text{Mn}_{1.57}\text{Fe}_{1.43}\text{O}_4$ nanoparticles in the liver is much higher than that of the other $\text{Mn}_x\text{Fe}_{3-x}\text{O}_4$ nanoparticles, suggesting that $\text{Mn}_x\text{Fe}_{3-x}\text{O}_4$ nanoparticles with high-Mn doping concentrations can efficiently accumulate in the liver. Early studies have revealed that hepatocytes can uptake the Mn^{2+} *via* vitamin B₆ transporters selectively [40]. Our previous work [7] has also proven that the accumulation of ultrasmall $\text{Mn}_x\text{Fe}_{3-x}\text{O}_4$ nanoparticles in the liver can be attributed to hepatocyte-specific uptake, while traditional superparamagnetic iron oxide nanoparticles were mostly localized in Kupffer cells. Therefore, it is reasonable to believe that the Mn^{2+} concentration on the surface of ultrasmall $\text{Mn}_x\text{Fe}_{3-x}\text{O}_4$ nanoparticles plays a significant role in its accumulation in the liver due to hepatocyte-specific uptake, although the detailed molecular mechanism still needs to be revealed. The accumulation amounts of the $\text{Mn}_x\text{Fe}_{3-x}\text{O}_4$ nanoparticles in the liver correspond well to their respective ΔSNRs in the liver, indicating that the *in vivo* contrast ability is determined by the *in vivo* accumulation of the nanoparticles rather than their *in vitro* r_1 relaxivity in this case.

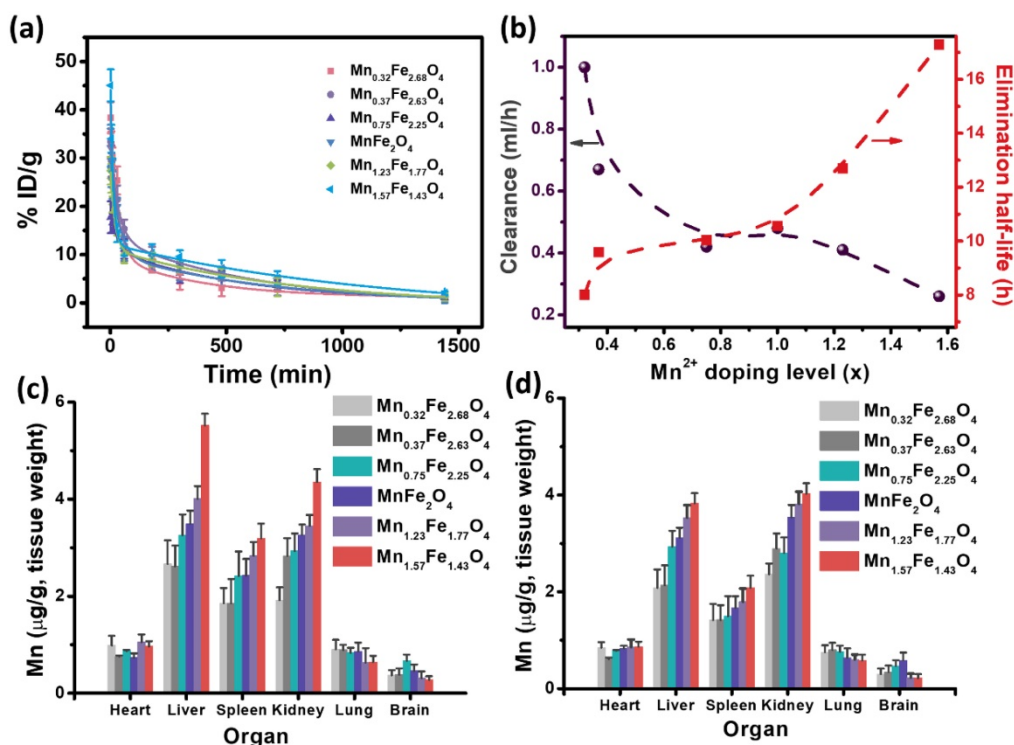


Figure 6. *In vivo* behaviors of ultrasmall $Mn_xFe_{3-x}O_4$ nanoparticles as determined by measuring Mn levels with ICP-MS. (a) Blood circulation of ultrasmall $Mn_xFe_{3-x}O_4$ nanoparticles. The pharmacokinetics of ultrasmall $Mn_xFe_{3-x}O_4$ nanoparticles followed the two-compartment model. (b) Correlation of elimination half-life and clearance of ultrasmall $Mn_xFe_{3-x}O_4$ nanoparticles. (c, d) Biodistribution of ultrasmall $Mn_xFe_{3-x}O_4$ nanoparticles in Balb/c mice at (c) 3 h and (d) 24 h post injection.

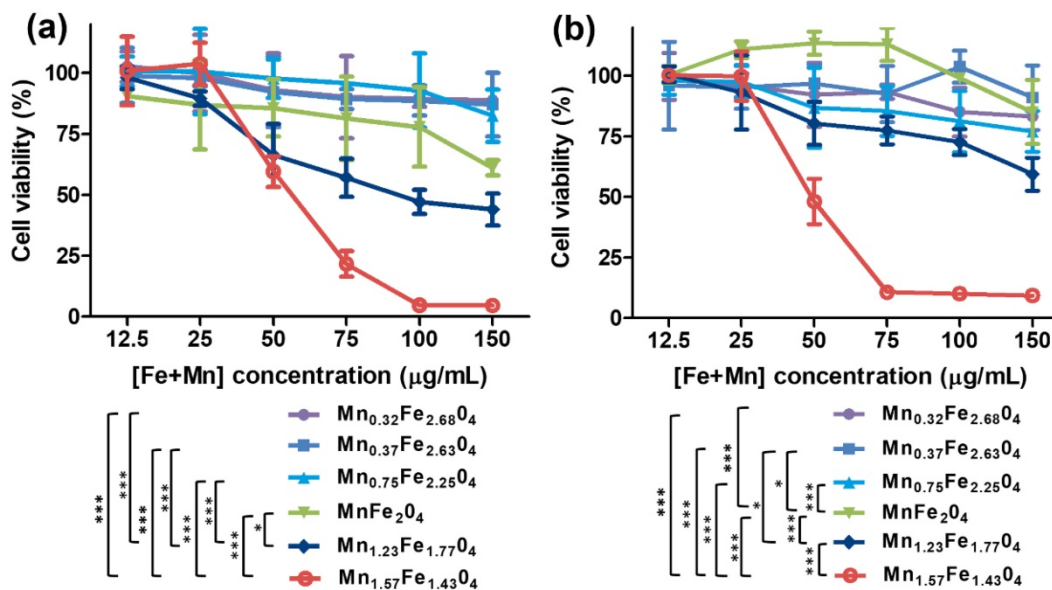


Figure 7. Relative viabilities of (a) Chang liver cells and (b) HepG2 cells incubated with ultrasmall $Mn_xFe_{3-x}O_4$ nanoparticles at various concentrations using standard cck-8 colorimetric assays. Error bars = SEM; * $p < 0.05$; ** $p < 0.01$; *** $p < 0.001$. p value is used to statistically analyze difference among groups at the [Fe+Mn] concentration of 50 $\mu\text{g/mL}$.

In Vitro and In Vivo Biosafety Evaluation

To assess the biosafety of the $Mn_xFe_{3-x}O_4$ nanoparticles, *in vitro* cell cytotoxicity assays, *in vivo* blood routine examination, blood biochemistry test and H&E staining examination were conducted using Balb/c mice. A cck-8 colorimetric assay using Chang

liver cells and HepG2 cells were performed to evaluate the cytotoxicity of the UMFNPs (Figure 7). The viabilities of the Chang liver cells exceed 80% at a high [Fe+Mn] concentration of 150 $\mu\text{g/mL}$ for the $Mn_{0.32}Fe_{2.68}O_4$, $Mn_{0.37}Fe_{2.63}O_4$ and $Mn_{0.75}Fe_{2.25}O_4$ nanoparticles after incubating for 24 h. In contrast, the viabilities of the Chang liver cells are less than 70% at

[Fe+Mn] concentrations higher than 50 $\mu\text{g}/\text{mL}$ for the $\text{Mn}_{1.23}\text{Fe}_{1.77}\text{O}_4$ and $\text{Mn}_{1.57}\text{Fe}_{1.43}\text{O}_4$ nanoparticles after incubating for 24 h. These results indicate that ultrasmall $\text{Mn}_x\text{Fe}_{3-x}\text{O}_4$ nanoparticles with high Mn-doping levels ($x = 1.23$ and 1.57) can induce significant cytotoxicity in Chang liver cells. Similar results were observed in HepG2 cells. The viabilities of HepG2 cells are higher than 80% at a high [Fe+Mn] concentration of 150 $\mu\text{g}/\text{mL}$ for the $\text{Mn}_{0.32}\text{Fe}_{2.68}\text{O}_4$, $\text{Mn}_{0.37}\text{Fe}_{2.63}\text{O}_4$ and $\text{Mn}_{0.75}\text{Fe}_{2.25}\text{O}_4$ nanoparticles, while the viabilities of HepG2 cells decreased to 50% at a [Fe+Mn] concentration of only 50 $\mu\text{g}/\text{mL}$ for the $\text{Mn}_{1.57}\text{Fe}_{1.43}\text{O}_4$ nanoparticles. For the *in vivo* biosafety investigation, mice were intravenously injected with $\text{Mn}_x\text{Fe}_{3-x}\text{O}_4$ nanoparticles at a dosage of 3 mg [Fe+Mn]/kg. After a 24 h circulation time, the whole blood, serum and liver were obtained for the blood routine examination, blood biochemistry tests and H&E staining examinations, respectively. Figure 8a-h shows the blood routine examination results of the $\text{Mn}_x\text{Fe}_{3-x}\text{O}_4$ nanoparticles, including values for the red blood cells (RBC), hemoglobin (HGB), white blood cells (WBC), hematocrit (HCT), mean corpuscular hemoglobin (MCH), mean corpuscular hemoglobin concentration (MCHC), platelets (PLT) and mean corpuscular volume (MCV). These markers are within the normal range without any observable difference from those of the mice in the control group, suggesting good hemocompatibility for the $\text{Mn}_x\text{Fe}_{3-x}\text{O}_4$ nanoparticles. For the blood biochemistry tests, important hepatic function indicators, such as the alanine transferase (ALT), aspartate transferase (AST), total protein (TP), albumin (ALB), total biliary acid (TBA), direct bilirubin (DBIL) and alkaline phosphatase (ALP) values, were investigated. As shown in Figure 8i-o, no significant difference in the levels of these markers compared to the control are observed for the $\text{Mn}_{0.32}\text{Fe}_{2.68}\text{O}_4$, $\text{Mn}_{0.37}\text{Fe}_{2.63}\text{O}_4$, $\text{Mn}_{0.75}\text{Fe}_{2.25}\text{O}_4$ and MnFe_2O_4 nanoparticles, indicating a good hepatic safety profile for these nanoparticles. However, the TBA and DBIL values of the $\text{Mn}_{1.23}\text{Fe}_{1.77}\text{O}_4$ and $\text{Mn}_{1.57}\text{Fe}_{1.43}\text{O}_4$ nanoparticles treated groups were much higher than those of the other $\text{Mn}_x\text{Fe}_{3-x}\text{O}_4$ nanoparticles treated groups and the control group. Nanoparticles can be cleared through the liver into the bile, and the levels of TBA and DBIL reflect the liver functions of excretion, secretion and detoxification [41, 42]. The increased TBA and DBIL values imply a potential toxicity towards the functions of the liver caused by the increasing manganese content. The cellular internalization of $\text{Mn}_x\text{Fe}_{3-x}\text{O}_4$ may trigger the partial dissolution of the nanoparticles, leading to the release of Mn ions. The toxicity of Mn ions results from the variable valence states of Mn and its disruption of the homeostasis of

pro-oxidant and antioxidant factors, which leads to toxic damage [43, 44]. To further evaluate the potential tissue damage, inflammation or lesions in the liver that $\text{Mn}_x\text{Fe}_{3-x}\text{O}_4$ nanoparticles may cause, H&E staining examinations were conducted. As shown in Figure 9, compared with those of the control group, the tissue structures of the livers from mice treated with $\text{Mn}_x\text{Fe}_{3-x}\text{O}_4$ nanoparticles remain intact, and no abnormal changes in the pathological histology or cellular structures are observed in the livers after 1 day, indicating no obvious risks of the $\text{Mn}_x\text{Fe}_{3-x}\text{O}_4$ nanoparticles toward the liver. These results suggest that $\text{Mn}_{0.32}\text{Fe}_{2.68}\text{O}_4$, $\text{Mn}_{0.37}\text{Fe}_{2.63}\text{O}_4$, $\text{Mn}_{0.75}\text{Fe}_{2.25}\text{O}_4$ and MnFe_2O_4 , which have insignificant toxicities, are suitable for *in vivo* MRI.

The chemical design of nanoparticle-based contrast agents is typically highly concentrated to maximize the relaxivity. However, the optimization of a single factor is insufficient to predict the *in vivo* contrast efficacy. The nano-bio interactions and *in vivo* safety should also be taken into account for maximizing the *in vivo* contrast efficacy. Based on the above experimental results, the Mn-doping level of $\text{Mn}_x\text{Fe}_{3-x}\text{O}_4$ nanoparticles can simultaneously impact the *in vitro* T_1 relaxivity, the accumulation of nanoparticles in the liver and the biosafety. The key correlations between the chemical composition and the *in vitro* T_1 relaxivity, *in vivo* nano-bio interactions, and toxicity should be considered together. As shown in Figure 10, as the Mn-doping level increases, the T_1 relaxivity initially increases to $10.36 \text{ mM}^{-1}\text{s}^{-1}$ ($x = 0.75$) and then gradually decreases to $7.66 \text{ mM}^{-1}\text{s}^{-1}$ ($x = 1.57$), and both the ΔSNR and the particle accumulation in the liver increased. However, the *in vitro* cell viability and the liver functions of excretion, secretion and detoxification are adversely impacted by an increase in the Mn-doping level. The comparison and correlation analysis suggest that $\text{Mn}_x\text{Fe}_{3-x}\text{O}_4$ nanoparticles with Mn contents ranging from 0.75 to 1, have significantly improved *in vivo* contrast efficacies, and can be potential contrast agents for clinical liver-specific MRI.

Conclusions

In summary, 3 nm $\text{Mn}_x\text{Fe}_{3-x}\text{O}_4$ nanoparticles with tunable Mn-doping levels ($x = 0.32, 0.37, 0.75, 1, 1.23$ and 1.57) have been successfully synthesized *via* a DSTD method. These $\text{Mn}_x\text{Fe}_{3-x}\text{O}_4$ nanoparticles were used as a model system to systematically investigate the correlation between chemical composition and *in vivo* T_1 contrast efficacy. The results suggest that variations in the Mn contents of $\text{Mn}_x\text{Fe}_{3-x}\text{O}_4$ nanoparticles can effectively impact *in vitro* T_1 relaxivities, *in vivo* nano-bio interactions and toxicities simultaneously. The relationships between the

chemical composition and each individual factor have been revealed. It was found that with increasing Mn-doping levels in the $Mn_xFe_{3-x}O_4$ nanoparticles, the T_1 relaxivities initially increased and then declined, while the *in vivo* MR signals increased linearly, along with an adverse increase in their toxicities. A comparison analysis of these given relationships indicated that the $Mn_xFe_{3-x}O_4$ ($x = 0.75-1$) nanoparticles, as UFNP-based contrast agents,

exhibited the optimal *in vivo* contrast efficacy for liver-specific MRI. The principles identified in this work and multiple factor assessment used herein can be applied to optimize other UFNPs for high-performance contrast-enhanced MRI. We believe this work represents an essential step towards the development of high-efficiency and low-toxicity UFNP-based contrast agents for both fundamental research and clinical translation.

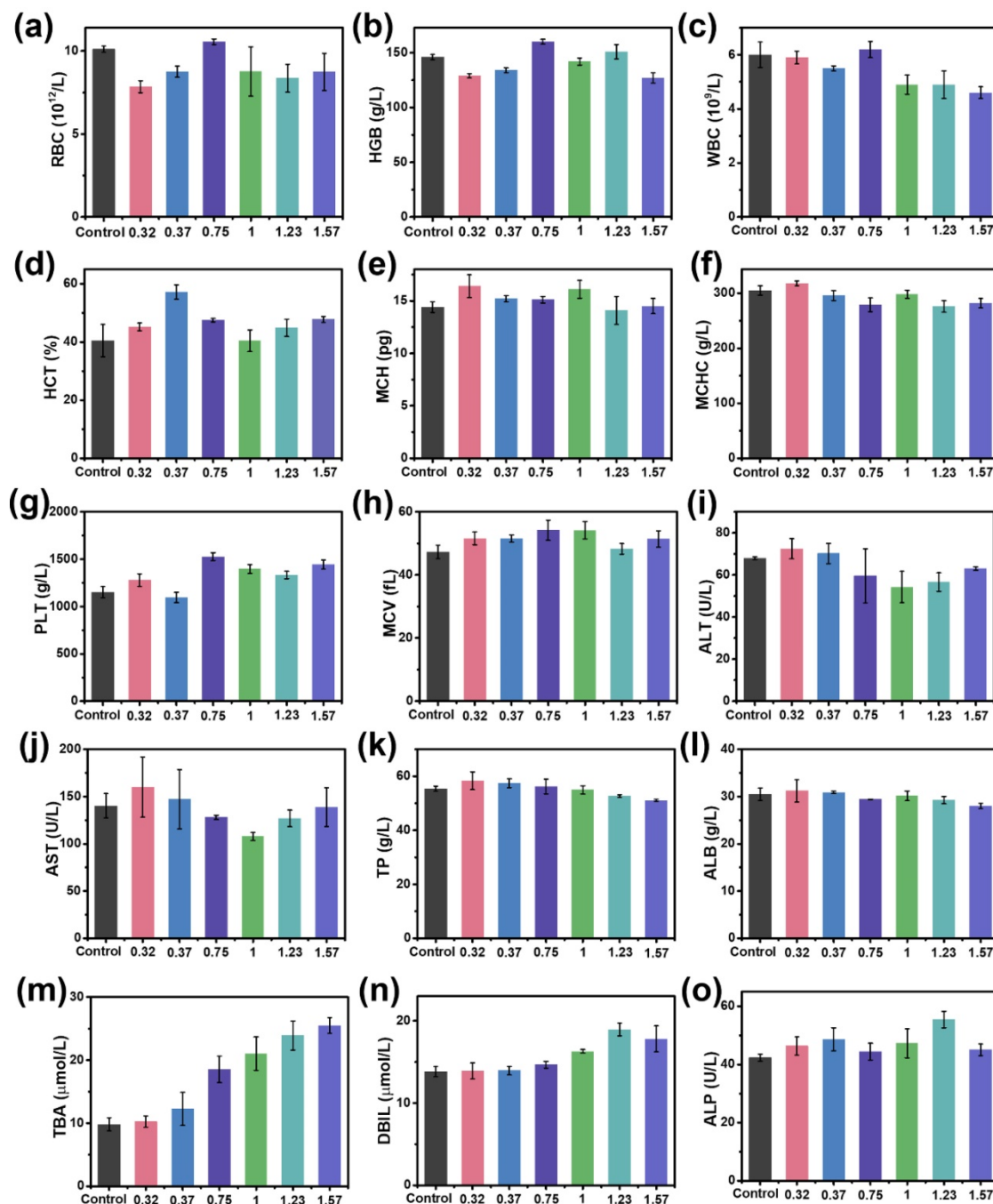


Figure 8. *In vivo* biosafety assessment of ultrasmall $Mn_xFe_{3-x}O_4$ nanoparticles. (a–h) Routine blood analysis: (a) red blood cells (RBC), (b) hemoglobin (HGB), (c) white blood cell (WBC), (d) hematocrit (HCT), (e) mean corpuscular hemoglobin (MCH), (f) mean corpuscular hemoglobin concentration (MCHC), (g) platelets (PLT) and (h) mean corpuscular volume (MCV); (i–o) Blood biochemistry test: (i) alanine transferase (ALT), (j) aspartate transferase (AST), (k) total protein (TP), (l) albumin (ALB), (m) total biliary acid (TBA), (n) direct bilirubin (DBIL) and (o) alkaline phosphatase (ALP).

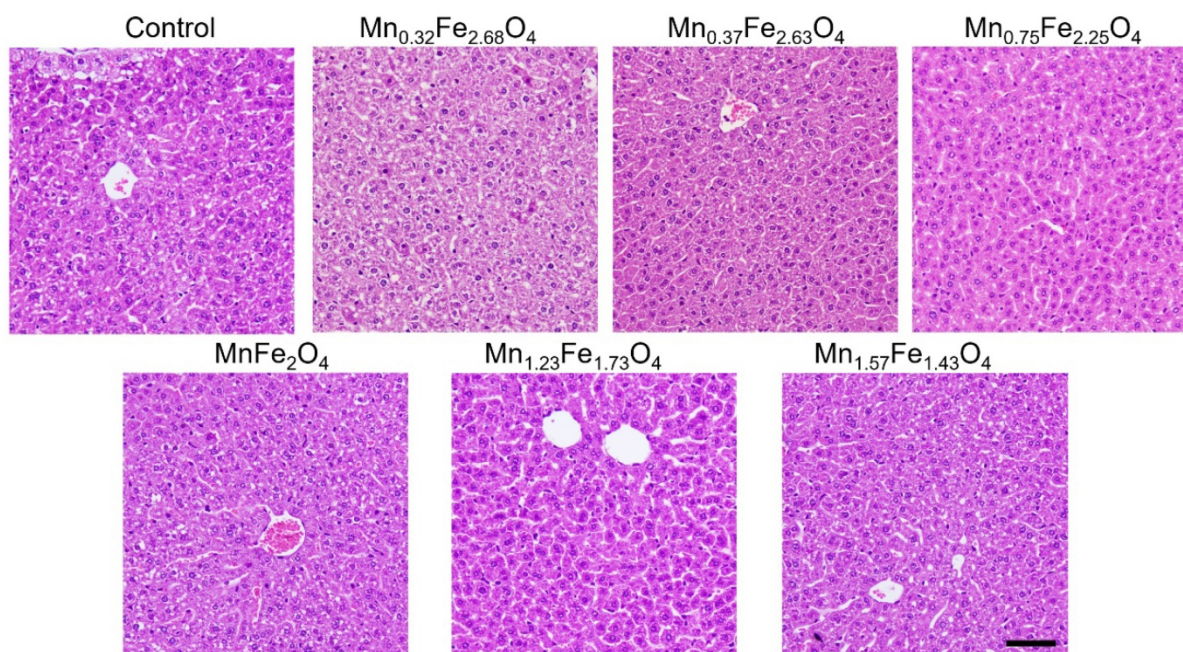


Figure 9. H&E stained images of the liver of the mice harvested from control group and treated groups at 1 days after intravenous injection of ultrasmall $Mn_xFe_{3-x}O_4$ nanoparticles. Scale bar = 100 nm.

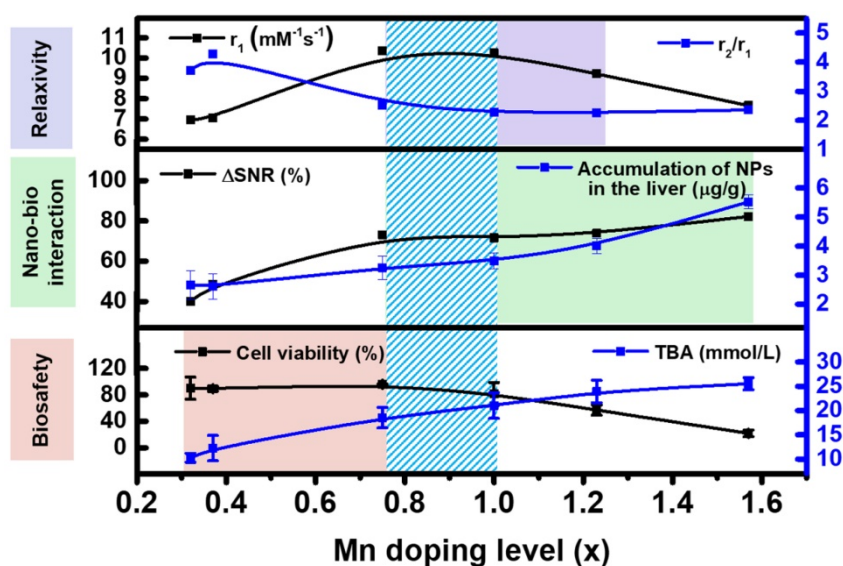


Figure 10. The comparison and correlation analysis of Mn concentration with *in vitro* T_1 relaxivity, *in vivo* nano-bio interactions and biosafety.

Abbreviations

ALT: alanine transferase; ALP: alkaline phosphatase; ALB: albumin; AST: aspartate transferase; CL: clearance; DSTD: dynamic simultaneous thermal decomposition; DLS: dynamic light scattering; DBIL: direct bilirubin; HCT: hematocrit; HGB: hemoglobin; MRI: magnetic resonance imaging; MCH: mean corpuscular hemoglobin; MCHC: mean corpuscular hemoglobin concentration; MCV: mean corpuscular volume; PLT: platelets; RBC: red blood cells; SQUID: superconducting quantum interference device; TBA:

total biliary acid; TEM: transmission electron microscopy; TP: total protein; UFNPs: ultrasmall ferrite nanoparticles; UMFNPs: ultrasmall manganese ferrite nanoparticles; WBC: white blood cell; XRD: X-ray powder diffraction; XPS: X-ray photoelectron spectroscopy.

Supplementary Material

Supplementary figures and tables.

<http://www.thno.org/v09p1764s1.pdf>

Acknowledgments

The authors thank the financial support provided by National Natural Science Foundation of China (Grant Nos. 81571809, 81771981, and 81300199).

Competing Interests

The authors have declared that no competing interest exists.

References

- Kim BH, Lee N, Kim H, An K, Park YI, Choi Y, et al. Large-scale synthesis of uniform and extremely small-sized iron oxide nanoparticles for high-resolution T₁ magnetic resonance imaging contrast agents. *J Am Chem Soc.* 2011; 133: 12624-31.
- Li Z, Yi PW, Sun Q, Lei H, Li Zhao H, Zhu ZH, et al. Ultrasmall water-soluble and biocompatible magnetic iron oxide nanoparticles as positive and negative dual contrast agents. *Adv Funct Mater.* 2012; 22: 2387-93.
- Lu Y, Xu YJ, Zhang GB, Ling D, Wang MQ, Zhou Y, et al. Iron oxide nanoclusters for T₁ magnetic resonance imaging of non-human primates. *Nat Biomed Eng.* 2017; 1: 637-43.
- Taboada E, Rodri'guez E, Roig A, Oro' J, Roch A, Muller RN. Relaxometric and magnetic characterization of ultrasmall iron oxide nanoparticles with high magnetization evaluation as potential T₁ magnetic resonance imaging contrast agents for molecular imaging. *Langmuir.* 2007; 23: 4583-8.
- Tromsdorf UI, Bruns OT, Salmen SC, Beisiegel U, Weller H. A highly effective, nontoxic T₁ MR contrast agent based on ultrasmall PEGylated iron oxide nanoparticles. *Nano Lett.* 2009; 9: 4434-40.
- Wei H, Bruns OT, Kaul MG, Hansen EC, Barch M, Wisniewska A, et al. Exceedingly small iron oxide nanoparticles as positive MRI contrast agents. *Proc Natl Acad Sci U S A.* 2017; 114: 2325-30.
- Zhang H, Li L, Liu XL, Jiao J, Ng CT, Yi JB, et al. Ultrasmall ferrite nanoparticles synthesized via dynamic simultaneous thermal decomposition for high-performance and multifunctional T₁ magnetic resonance imaging contrast agent. *ACS Nano.* 2017; 11: 3614-31.
- Li Z, Wang SX, Sun Q, Zhao HL, Lei H, Lan MB, et al. Ultrasmall manganese ferrite nanoparticles as positive contrast agent for magnetic resonance imaging. *Adv Healthc Mater.* 2013; 2: 958-64.
- Chen R, Ling D, Zhao L, Wang S, Liu Y, Bai R, et al. Parallel comparative studies on mouse toxicity of oxide nanoparticle- and gadolinium-based T₁ MRI contrast agents. *ACS Nano.* 2015; 9: 12425-35.
- Shen Z, Chen T, Ma X, Ren W, Zhou Z, Zhu G, et al. Multifunctional theranostic nanoparticles based on exceedingly small magnetic iron oxide nanoparticles for T₁-weighted magnetic resonance imaging and chemotherapy. *ACS Nano.* 2017; 11: 10992-1004.
- Wang L, Wu Q, Tang S, Zeng J, Qiao R, Zhao P, et al. Ultrasmall PEGylated Mn₃Fe_{3-x}O₄ (x = 0-0.34) nanoparticles: effects of Mn(II) doping on T₁- and T₂-weighted magnetic resonance imaging. *RSC Advances.* 2013; 3: 23454-60.
- Shen Z, Song J, Zhou Z, Yung BC, Aronova MA, Li Y, et al. Dotted core-shell nanoparticles for T₁-weighted MRI of tumors. *Adv Mater.* 2018; 30: 1803163-73.
- Zeng J, Jing L, Hou Y, Jiao M, Qiao R, Jia Q, et al. Anchoring group effects of surface ligands on magnetic properties of Fe₃O₄ nanoparticles: towards high performance MRI contrast agents. *Adv Mater.* 2014; 26: 2694-8.
- Boselli L, Polo E, Castagnola V, Dawson KA. Regimes of biomolecular ultrasmall nanoparticle interactions. *Angew Chem Int Ed Engl.* 2017; 56: 4215-8.
- Polo E, Collado M, Pelaz B, Del Pino P. Advances toward more efficient targeted delivery of nanoparticles in vivo: understanding interactions between nanoparticles and cells. *ACS Nano.* 2017; 11: 2397-402.
- Shi J, Kantoff PW, Wooster R, Farokhzad OC. Cancer nanomedicine: progress, challenges and opportunities. *Nat Rev Cancer.* 2017; 17: 20-37.
- Stark WJ. Nanoparticles in biological systems. *Angew Chem Int Ed Engl.* 2011; 50: 1242-58.
- Wilhelm S, Tavares AJ, Dai Q, Ohta S, Audet J, Dvorak HF, et al. Analysis of nanoparticle delivery to tumours. *Nat Rev Mater.* 2016; 1.
- Arami H, Khandhar A, Liggitt D, Krishnan KM. In vivo delivery, pharmacokinetics, biodistribution and toxicity of iron oxide nanoparticles. *Chem Soc Rev.* 2015; 44: 8576-607.
- Kang H, Gravier J, Bao K, Wada H, Lee JH, Baek Y, et al. Renal clearable organic nanocarriers for bioimaging and drug delivery. *Adv Mater.* 2016; 28: 8162-8.
- Yang Y, Liu J, Liang C, Feng L, Fu T, Dong Z, et al. Nanoscale metal-organic particles with rapid clearance for magnetic resonance imaging-guided photothermal therapy. *ACS Nano.* 2016; 10: 2774-81.
- Zhou Z, Wang L, Chi X, Bao J, Yang L, Zhao W, et al. Engineered iron-oxide-based nanoparticles as enhanced T₁ contrast agents for efficient tumor imaging. *ACS Nano.* 2013; 7: 3287-96.
- Yang L, Ma L, Xin J, Li A, Sun C, Wei R, et al. Composition tunable manganese ferrite nanoparticles for optimized T₂ contrast ability. *Chem Mater.* 2017; 29: 3038-47.
- Chabanova E, Logager VB, Moller JM, Thomsen HS. Manganese based MR contrast agents: formulation and clinical applications. *The Open Drug Safety Journal.* 2011; 2: 29-38.
- Liu XL, Fan HM, Yi JB, Yang Y, Choo ESG, Xue JM, et al. Optimization of surface coating on Fe₃O₄ nanoparticles for high performance magnetic hyperthermia agents. *J Mater Chem.* 2012; 22: 8235-44.
- Xu Y, Sherwood J, Qin Y, Holler RA, Bao Y. A general approach to the synthesis and detailed characterization of magnetic ferrite nanocubes. *Nanoscale.* 2015; 7: 12641-9.
- Wu T, Zhao Y, Li Y, Wu W, Tong G. Controllable synthesis of Cu₃Fe_{3-x}O₄@Cu core-shell hollow spherical chains for broadband, lightweight microwave absorption. *ChemCatChem.* 2017; 9: 3486-96.
- Carta D, Casula MF, Falqui A, Locher D, Mountjoy G, Sangregorio C, et al. A structural and magnetic investigation of the inversion degree in ferrite nanocrystals MFe₂O₄ (M = Mn, Co, Ni). *J Phys Chem C.* 2009; 113: 8606-15.
- J W, Yejun W, Yuejin Z. Cation distribution of MnFe₂O₄ nanoparticles synthesized under an induced magnetic field. *Int J Mod Phys B.* 2007; 21: 723-9.
- Giri J, Pradhan P, Somani V, Chelawat H, Chhatre S, Banerjee R, et al. Synthesis and characterizations of water-based ferrofluids of substituted ferrites [Fe_{1-x}B_xFe₂O₄, B = Mn, Co (x = 0-1)] for biomedical applications. *J Magn Magn Mater.* 2008; 320: 724-30.
- Giri J, Pradhan P, Sriharsha T, Bahadur D. Preparation and investigation of potentiality of different soft ferrites for hyperthermia applications. *J App Phys.* 2005; 97.
- van der Zaag PJ, Noordermeer A, Johnson MT, Bongers PF. Comment on "Size-dependent Curie temperature in nanoscale MnFe₂O₄ particles". *Phys Rev Lett.* 1992; 68: 3112.
- Lauffer RE. Paramagnetic metal complexes as water proton relaxation agents for NMR imaging: theory and design. *Chem Rev.* 1987; 87: 901-27.
- Ni D, Bu W, Ehlerding EB, Cai W, Shi J. Engineering of inorganic nanoparticles as magnetic resonance imaging contrast agents. *Chem Soc Rev.* 2017; 46: 7438-68.
- Huang J, Bu L, Xie J, Chen K, Cheng Z, Li X, et al. Effects of nanoparticle size on cellular uptake and liver MRI with polyvinylpyrrolidone-coated iron oxide nanoparticles. *ACS Nano.* 2010; 4: 7151-60.
- Yu M, Zheng J. Clearance pathways and tumor targeting of imaging nanoparticles. *ACS Nano.* 2015; 9: 6655-74.
- Du B, Jiang X, Das A, Zhou Q, Yu M, Jin R, et al. Glomerular barrier behaves as an atomically precise bandpass filter in a sub-nanometre regime. *Nat Nanotechnol.* 2017; 12: 1096-102.
- Greenblatt DJ. Elimination half-life of drugs: value and limitations. *Annu Rev Med.* 1985; 36: 421.
- Xu J, Yu M, Peng C, Carter P, Tian J, Ning X, et al. Dose dependencies and biocompatibility of renal clearable gold nanoparticles: from mice to non-human primates. *Angew Chem Int Ed.* 2018; 57: 266-71.
- Semelka RC, Helmberger TKG. Contrast agents for MR imaging of the liver. *Radiology.* 2001; 218: 27-38.
- Wang L, Wu G, Wu F, Jiang N, Lin Y. Geniposide attenuates ANIT-induced cholestasis through regulation of transporters and enzymes involved in bile acids homeostasis in rats. *J Ethnopharmacol.* 2017; 196: 178-85.
- Yan JY, Ai G, Zhang XJ, Xu HJ, Huang ZM. Investigations of the total flavonoids extracted from flowers of *Abelmoschus manihot* (L.) Medic against alpha-naphthylisothiocyanate-induced cholestatic liver injury in rats. *J Ethnopharmacol.* 2015; 172: 202-13.
- Blazk WF, Brown GL, Treinen KA, Denny KH. Developmental toxicity study of mangafodipir trisodium injection (MnDPDP) in new zealand white rabbits. *Toxicological Sciences.* 1996; 33: 11-5.
- O'Neal SL, Zheng W. Manganese toxicity upon overexposure: a decade in review. *Curr Environ Health Rep.* 2015; 2: 315-28.